Simulation of the discharge and microwave-plasma coupling in a waveguide ECR thruster

IEPC-2024-592

Presented at the 38th International Electric Propulsion Conference, Toulouse, France
June 23-28, 2024

M. R. Inchingolo * P. Jimenez † J. Zhou ‡ M. Merino § and J. Navarro-Cavallé¶
Department of Aerospace Engineering, Universidad Carlos III de Madrid, Madrid, 28911, Spain

A circular waveguide electron-cyclotron resonance thruster (ECRT) is simulated using a quasi-neutral 2D axisymmetric hybrid PIC-fluid-wave code. Plasma heating is incorporated through a heating term in the fluid energy equation for electrons. This term is computed by a dedicated module that simulates the propagation and absorption of electromagnetic fields in the plasma with arbitrary azimuthal modes, m. We investigate the plasma property profiles, the propulsive performance, the wave propagation and absorption in the discharge chamber and near plume, and the reflection coefficient for the modes $m = \pm 1$. Two configurations, with radial and axial propellant injection respectively, are considered. Different wave propagating regimes are found to exist within the discharge chamber, depending on the plasma density and magnetic field conditions. Both azimuthal modes can contribute significantly to the absorbed power, with $m = +1$ being dominant, particularly in the axial injection case. Higher performance metrics are observed for the axial injection configuration, which exhibits lower losses to the thruster walls and higher utilization efficiency.

I. Introduction

The electron cyclotron resonance thruster (ECRT) is an electrodeless plasma thruster that exploits the ECR resonance to efficiently couple electromagnetic power to the plasma electrons. The plasma is externally expanded in a magnetic nozzle (MN), generating magnetic thrust.

Waveguide-coupled ECRT thrusters were first investigated from the 1960s to the 1990s, with thrusters in the kW power range [1, 2]. Thruster efficiencies never exceeded 10%, resulting in the technology being abandoned in favor of more promising alternatives. Distinct from the waveguide ECRT type, in recent years, a novel coaxial ECRT thruster geometry was developed at ONERA [3], and, with the recent development, efficiencies as high as 50% were reported (2.45 GHz, 35 W, and 0.8 sccm of Xenon) [4]. These promising results further pushed the interest in the ECRT concept.

Recently, a new waveguide-based ECRT has been developed and characterized experimentally at Universidad Carlos III de Madrid [5, 6] to elucidate the limitations encountered in past waveguide ECRT designs and devise strategies to overcome them. Experiments conducted on this thruster identified substantial losses, and an efficiency below 3.5% was observed (5.8 GHz, 60 W, and 2 sccm of Xenon)[6]. In this regard, plasma discharge simulations can come in useful to comprehend the loss mechanisms characterizing this type of thruster: simulations offer the potential to access information on plasma quantities that are experimentally challenging to obtain or inaccessible, conversely, experiments provide the data required to corroborate and validate these simulations.

*PhD, minching@pa.uc3m.es
†PhD, pejimene@ing.uc3m.es
‡Assistant professor, jzhou@pa.uc3m.es
§Full professor, mario.merino@uc3m.es
¶Associate professor, janavarr@ing.uc3m.es

Copyright 2024 by the Electric Rocket Propulsion Society. All rights reserved.

Different quasi-1D models were proposed in the past obtaining in some cases good estimations of the thruster performance for coaxial ECRTs [2, 7]. However, a deeper understanding of the discharge physics in an ECRT cannot be obtained without modeling microwave-plasma coupling, fundamental for determining power absorption location. Building on the hybrid PIC-Fluid code (HYPHEN-EPT)[8, 9], recent upgrades have gradually enabled the coupled computation of the (slow) plasma transport and the (fast) electromagnetic fields in EPT devices. In [10], Sánchez-Villar et al. used HYPHEN plus an MFEM-based wave code to simulate a coaxial ECRT, which exhibits only an azimuthal $m = 0$ mode. This code models the electromagnetic fields in the frequency domain, considering the linear cold-plasma dielectric response. In [11], the first effort to simulate the waveguide ECRT concept was made. As the capability to simulate modes different from $m = 0$ was not available at the time, the microwave power deposition profile in the circular waveguide discharge chamber was prescribed to be near the ECR region. This approach, while not self-consistent, provided a preliminary understanding of the discharge physics of the ECRT prototype. More recently, a new wave solver module based on FENICSx has been coupled to HYPHEN. This module, which otherwise implements the same physical model as in [10], allows simulating the propagation and absorption of electromagnetic power within the plasma on any m mode. This strategy has been successfully used (and validated) in simulating the discharge physics of Helicon thrusters [12].

The objective of this work is to present the first self-consistent plasma-wave simulations of a waveguide ECRT. We investigate the plasma properties profiles, the propulsive performance, the wave propagation and absorption in the discharge chamber and near plume, the power deposition maps, and the reflection coefficient for the $m = \pm 1$ modes. Two configurations, with radial and axial propellant injection respectively, are considered. The existence of different parametric regimes for wave propagation leads to different locations for power absorption within the discharge chamber for the two cases.

The rest of the document is organized as follows: in section II the HYPHEN model and structure are presented, with particular emphasis on the new wave propagation module (section IIA). In section III the results are presented first with a focus on the radial propellant injection case, taken as a reference (section IIIA) then in section IIIB the axial injection configuration and its potential advantages are presented. Section IV summarizes the conclusions of this work.

II. Model Description

Figure 1 shows the structure of HYPHEN. It has a modular structure and consists of a total of four modules: the heavy species (I) module, the electron fluid (E) module, the sheath (S) module, and the wave (W) module. The first three modules (I-E-S) [13, 14] implement the physics related to the (slow) plasma transport. The I-module is based on a Particle-In-Cell (PIC) model [13] for multiple heavy plasma species, including ions and neutrals, while the E-module employs a diffusive, magnetized fluid model [14] to solve for electron dynamics. The plasma is assumed quasi-neutral and the S-module solves the Debye sheath completing the electron solution at the thruster walls. The W-module [12] is tasked with solving the Maxwell equations for electromagnetic fields using a quasi-steady cold plasma dielectric tensor.

In figure 1 and in the following, the density and velocity of a heavy species s are denoted as n_s and $\boldsymbol{u}_s$; the electric potential, electron current density, electron temperature and heat flux as ϕ, $\boldsymbol{j}_e$, T_e and $\boldsymbol{q}_e$; and the power deposition density as Q_a. Within the transport module, the I-module and E-module are run sequentially. First, the I-module is advanced for a time step Δt, taking as inputs ϕ and T_e and providing n_s and $\boldsymbol{u}_s$ to the E-module. With the additional input of Q_a coming from the W-module, the E-module is advanced a number of sub-iterations N_e for each Δt, so that $\Delta t_e = \Delta t / N_e$. The E-module provides back ϕ and T_e to the I-module, closing the transport sub-loop. The W-module is called with the lowest frequency in the simulation loop, having a time step $\Delta t_w = N_w \Delta t$. This module takes as input the plasma density, n_e, the collisionality $\nu_e(n_s, T_e)$, and the static magnetic field map. These inputs are used to compute the cold plasma dielectric tensor and update the power deposition map Q_a. The obtained map is constantly provided to the E-module for the time frame between subsequent W-module calls.

Each module uses a different mesh. The I-module uses a Cartesian-type structured mesh, while the E-module uses a magnetic field-aligned mesh (MFAM), which minimizes the numerical diffusion of the magnetized anisotropic electrons. The W-module uses an unstructured mesh. Two reference systems are used, the cylindrical one defined by $\{\mathbf{1}_z, \mathbf{1}_r, \mathbf{1}_\theta\}$; and the magnetic one defined by $\{\mathbf{1}_\parallel, \mathbf{1}_\perp, \mathbf{1}_\theta\}$ with $\mathbf{1}_\parallel = \boldsymbol{B}/B$ and $-\mathbf{1}_\perp = \mathbf{1}_\parallel \times \mathbf{1}_\theta$. The I and W-modules use the first system while the E-module uses the second. Interpolation of the plasma magnitude maps is necessary from the different meshes [15, 14]

The 38th International Electric Propulsion Conference, P. Baudis Convention Center, Toulouse, France, June 23-28, 2024
Copyright 2024 by the Electric Rocket Propulsion Society. All rights reserved.

The transport modules were discussed several times in previous works, and more details can be found in [13, 14, 10, 16]. However, the W-module is a novelty, therefore it is further explained next in more detail.

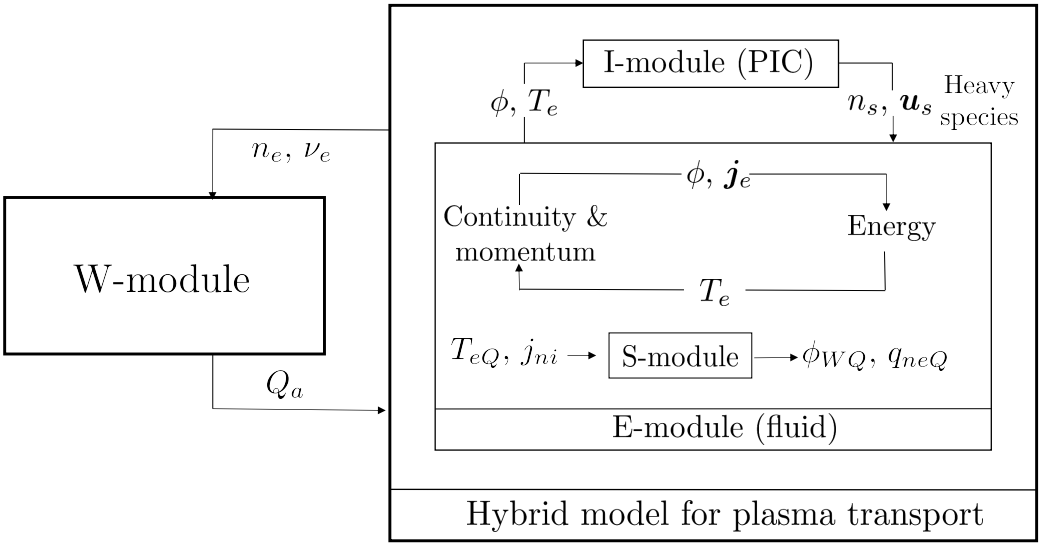

Figure 1: HYPHEN code structure.

IIA. Electromagnetic wave module

The PWHISTLER code, which here serves as the W-module, implements a full-wave, frequency-domain, linear cold-plasma model using a mixed Lagrange/vector finite element discretization on an unstructured grid. The details of the code are discussed in reference [12]. Shortly, the code solves the wave equation for an excitation frequency ω,

$$\nabla \times (\nabla \times \hat{\boldsymbol{E}}) - \frac{\omega^2}{c^2}\overline{\overline{\kappa}} \cdot \hat{\boldsymbol{E}} = \boldsymbol{0}, \tag{1}$$

$\hat{\boldsymbol{E}}$ is the complex magnitude of the electric field such that the time dependent field is $\boldsymbol{E} = \Re\left[\hat{\boldsymbol{E}} \exp(-i\omega t)\right]$, and $\overline{\overline{\kappa}}$ the dielectric tensor that incorporates the electron response to the fields. In the $\{\mathbf{1}_\parallel, \mathbf{1}_\perp, \mathbf{1}_\theta\}$ magnetically-aligned vector basis:

$$\overline{\overline{\kappa}}(z,r) = \begin{pmatrix} P & 0 & 0 \\ 0 & (R+L)/2 & -i(R-L)/2 \\ 0 & i(R-L)/2 & (R+L)/2 \end{pmatrix}, \tag{2}$$

with:

$$R = 1 - \frac{\omega_{pe}^2}{\omega(\omega + \mathrm{i}\nu_e - \omega_{ce})}, \qquad L = 1 - \frac{\omega_{pe}^2}{\omega(\omega + \mathrm{i}\nu_e + \omega_{ce})}, \qquad P = 1 - \frac{\omega_{pe}^2}{\omega(\omega + \mathrm{i}\nu_e)}.$$

In the GHz frequency range, the ion contribution to the induced plasma current is much lower than that of electrons and has been neglected. The primary plasma parameters in the electromagnetic model are the electron cyclotron frequency $\omega_{ce} = eB/m_e$, and the plasma frequency, $\omega_{pe} = \sqrt{ne^2/(m_e\varepsilon_0)}$. The 2D maps for the applied field B, the plasma density n, and the electron collisionality ν_e, are inputs to the W-module.

Dot multiplying equation (1) by a test function $\boldsymbol{T}$ [17] and integrating over the simulation domain Ω, the

Copyright 2024 by the Electric Rocket Propulsion Society. All rights reserved.

following weak form is finally obtained:

$$\iint_{\Sigma} \left\{ \left[\left(\tilde{\nabla} + \mathbf{1}_{\boldsymbol{\theta}} \frac{im}{r} \right) \times \boldsymbol{T}^{(m)} \right] \cdot \left[\left(\tilde{\nabla} - \mathbf{1}_{\boldsymbol{\theta}} \frac{im}{r} \right) \times \boldsymbol{E}^{(m)} \right] - k_0^2 \boldsymbol{T}^{(m)} \cdot \overline{\overline{\kappa}} \cdot \boldsymbol{E}^{(m)} \right\} \mathrm{d}S + \\ + ik_0 \int_{\delta\Sigma} \boldsymbol{T}^{(m)} \cdot \left[\boldsymbol{n} \times \left(\tilde{\nabla} - \mathbf{1}_{\boldsymbol{\theta}} \frac{im}{r} \right) \times \boldsymbol{E}^{(m)} \right] \mathrm{d}l = 0 \tag{3}$$

where $\tilde{\nabla}\times$ is following differential operator and $\boldsymbol{E}^{(m)}$ are $\boldsymbol{T}^{(m)}$ are the field vectors for azimuthal mode m:

$$\tilde{\nabla} \times \boldsymbol{F} = \frac{1}{r} \frac{\partial F_\theta}{\partial r} \mathbf{1}_{\boldsymbol{z}} - \frac{\partial F_r}{\partial z} \mathbf{1}_{\boldsymbol{r}} + \left(\frac{\partial F_r}{\partial z} - \frac{\partial F_z}{\partial r} \right) \mathbf{1}_{\boldsymbol{\theta}} \tag{4}$$

A mixed finite element discretization is then applied, using a Nédélec basis for (E_z, E_r) and a Lagrange basis for E_θ. This conforming mixed element technique has proven effective in preventing the artificial buildup of spurious currents [18, 19].

The boundary conditions are perfect electric conductor (PEC) for the lateral and top walls of the simulation domain. This imposes a null tangential electric field there, $\boldsymbol{n} \times \boldsymbol{E}^{(m)}$. Continuity conditions are applied on the axis of symmetry [12]. Additionally, waveport boundary conditions are used to prescribe an incoming wave from the known solution in the waveguide while allowing the escape of any reflected of power.

Finally, the time-averaged power deposition for each mode can be computed from the EM field solution. This map, interpolated to the corresponding mesh, is the input into the electron fluid energy equation.

$$Q_a^{(m)} = \frac{1}{2} \Re \left((\boldsymbol{E}^{(m)})^* \cdot \overline{\overline{\kappa}} \cdot \boldsymbol{E}^{(m)} \right). \tag{5}$$

Taking advantage of linearity, the contribution of each m mode can be solved independently, and then superposed.

$$Q_a = \sum_m Q_a^{(m)} \tag{6}$$

Again, using linearity, the total absorbed power $\int_\Sigma Q_a \mathrm{d}V$, and electromagnetic fields accordingly, can be scaled to the prescribed value in each simulation. Generally, this spectral method is computationally much faster than solving the 3D problem directly.

IIB. Simulation setup

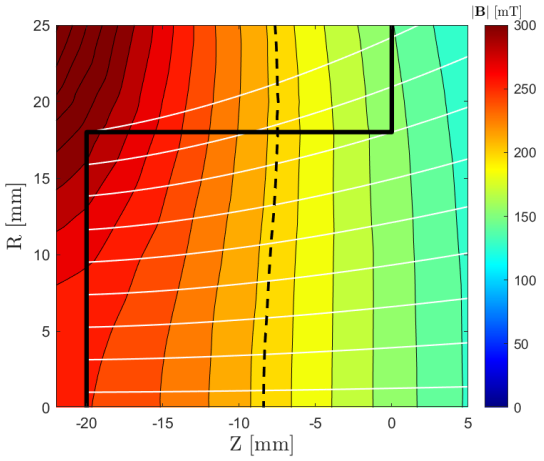

Figure 2: 2D section view of the ECRT magnetic field produced by the permanent magnet in the PC. White lines are magnetic field streamlines, the black dashed line represents the ECR layer, and the walls of the discharge chamber are shown with a black solid line.

Copyright 2024 by the Electric Rocket Propulsion Society. All rights reserved.

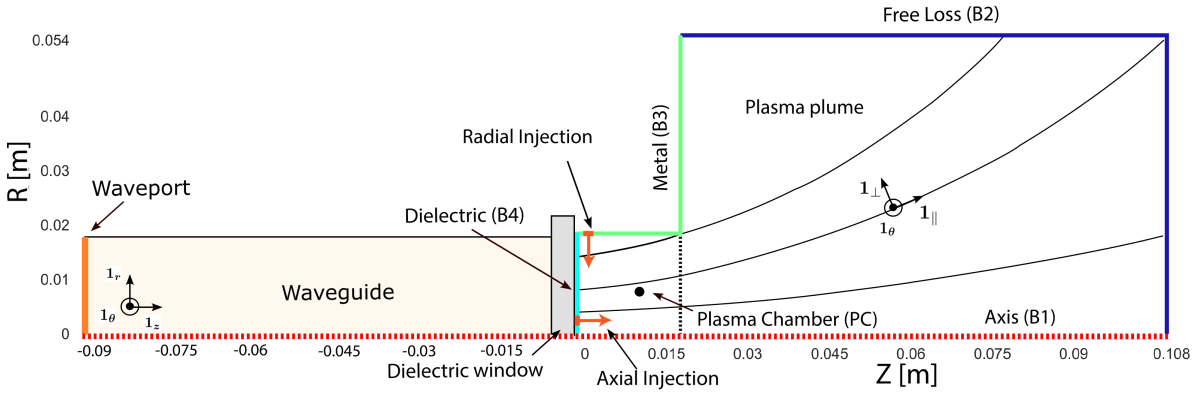

Figure 3: Scheme of the simulation domain and boundary conditions. The magnetic field streamlines are shown as solid black curves.

The waveguide ECRT used as a reference for the simulations here presented is a fully electrodeless circular waveguide thruster [5, 6]. The circular waveguide from which the microwaves are injected has a diameter of $D_T = 36$ mm, which at the input frequency $\omega = 5.8$ GHz allows the propagation of the TE_{11} mode only. The plasma chamber (PC) region, where the injected gas is ionized, consists of a semi-opened metallic tube, with one end closed by a quartz dielectric window to prevent the gas from flowing upstream. The PC keeps the same diameter as the waveguide and has a length of the $L_T = 20$ mm. At the operating frequency ω, the magnetic field required for the resonance is $B_{ECR} = 0.2$ T, therefore the PC is immersed in a static simply diverging magnetic field produced by a permanent magnet positioned behind the plasma chamber. Figure 2 displays the magnetic field produced by this magnet and the location of the resonance.

The simulation domain used by HYPHEN reproduces the dimensions and configuration of the experimental prototype. Figure 3 shows a scheme of the overall axisymmetric domain. From the left to the right, it can be found the circular waveguide region; the dielectric window; and the plasma domain region sum of the PC and plasma plume. While the W-module computes the solution of the electromagnetic wave propagation in the full domain shown, the transport modules operate only in the plasma domain.

Figure 3 also presents the location and type of boundary conditions used, these are chosen to reproduce closely the experimental conditions. The transport module uses four types of boundary conditions: axis (B1), free loss (B2), metallic (B3), and dielectric boundary (B4). Boundary conditions for the electron fluid model are applied following [14, 20]. B1 consists of an axisymmetric boundary condition, where both the electron fluxes are null. At the outwards boundary B2, a matching layer model is applied to the current-free plasma beam finite edge to obtain the electron currents and heat fluxes. At the thruster walls, a Debye sheath develops between the wall and the quasi-neutral plasma. A sheath model accounting for secondary electron emission and partial depletion of the tail of electron velocity distribution function is applied to connect conditions at the wall to those at the quasineutral plasma edge for $j_{ne} = \boldsymbol{j}_e \cdot \boldsymbol{n}$ and $q_{ne} = \boldsymbol{q}_e \cdot \boldsymbol{n}$, with $\boldsymbol{n}$ the unit normal pointing outwards of the domain. For dielectric walls (B4), $j_{ne} = j_{ni}$, while for metallic walls (B3) a floating condition is imposed $\int j_{ne} dS = \int j_{ni} dS$ obtaining a wall potential V_T. Regarding the PIC model, at B1 macroparticles are specularly reflected; at B2, macroparticles are removed from the domain; and at B3 and B4, ions and recombined, and the neutrals are reflected back to the domain. The angle after reflection is determined with the Schamberg model, and the energy is $E = E_{imp}(1 - \alpha_w) + 2T_w\alpha_w$ being: E_{imp} the impact energy, T_w the wall temperature and α_w) the accommodation factor. Many factors can influence in α_w) [21], and a value of $\alpha_w = 0.8$ was found to satisfactorily reproduce the low experimentally obtained utilization efficiency typical of this thruster prototype at the here presented working point. In addition, a value of $T_w = 250°$C is used, compatible with the temperatures reached during experimental testing.

Concerning the W-module, the wave port is positioned on the left of the waveguide. From this surface, the electromagnetic power is injected with two circularly polarized waves rotating in opposite directions at the frequency ω, corresponding to the modes $m = \pm 1$, together constituting a linearly polarized wave. As mentioned in section IIA, the input microwave power at the wave-port is scaled such that the total power absorbed by the plasma is $P_a = 175$ W.

Copyright 2024 by the Electric Rocket Propulsion Society. All rights reserved.

Parameter	Symbol	Value
Waveguide diameter	D_w	36 mm
Plasma chamber diameter	D_T	36 mm
Plasma Length	L_T	20 mm
Microwave frequency	ω	5.8 GHz
Resonance field	B_{ECR}	0.2 T
Injected mass flow rate (Xe)	$\dot{m}_p$	0.4 mg/s
Absorbed power	P_a	175 W
Ref. Injection location (z, r)	–	2 mm, 18 mm
Axial Injection location (z, r)	–	0 mm, 3 mm
I-module time-step	Δt	$2 \cdot 10^{-8}$
E-module time-step	Δt_e	$4 \cdot 10^{-9}$
W-module time-step	Δt_w	$2 \cdot 10^{-6}$
Total simulated time	t_{sim}	0.4 ms
Wall accommodation factor	α_w	0.8
Anomalous transport coefficient	α_{ANO}	0.1
Anomalous cooling coefficient	α_q	0.05

Table 1: Thruster design (upper part of the table) and simulation setup parameters (lower part of the table).

Except for the axis, the rest of the domain boundaries implement a Perfect Electric Conductor (PEC) condition. The dielectric window uses an isotropic relative permittivity of $\epsilon_r = 4.5$, whereas vacuum is assumed in the waveguide. As mentioned, the W-module uses an unstructured mesh, the latter is based on triangular elements, generated using the Gmsh open-source code. As we will see in the next sections, the nature of the problem leads to the formation of different wavelengths within the plasma. Therefore to save computational time, the typical mesh size in the waveguide and plume region is on the order of 1 mm whereas in the discharge chamber, the typical size is 10 μm.

In this work, two propellant injector positions are tested. In the reference case, the injector is positioned on the lateral metallic thruster walls at position $z = 2$ mm. A second injection location, positioned on the backplate at $r = 3$ mm, is also analyzed. The PIC particles injected are Xenon neutrals, with a mass flow rate of $\dot{m}_p = 0.4$ mg/s. During the simulation, single and double ions are produced through single ionization and double ionization inelastic collisions. Additionally, the simulations presented here implement excitation collisions, elastic collisions, and charge-exchange collisions [14].

Using the same notation as in [14], anomalous transport terms, α_{ano} and ν_q, are included in the momentum, energy, and heat flux equation for the E-module. These are used to model phenomenologically respectively, the electron instability-induced cross-field mobility, and the near-collisionless electron cooling. In this work, these parameters are chosen to be $\alpha_{ano} = 0.1$ and $\nu_q = 0.05$.

Table 1 displays in a compact format the above-discussed quantities.

All the plasma 2D maps here discussed are those obtained at steady state conditions, which is reached after $t_{ss} = 0.25$ ms (being $t = 0$ ms the time at which the fluid-pic models start to being solved together). The depicted plots correspond to averaged quantities for a time period of 0.15 ms.

III. Results

IIIA. Reference Case

The reference case for these simulations is set at a working point of $P_T = 175$ W and $\dot{m}_p = 4$ sccm, with the Xenon propellant injected radially near the backplate. The availability of performance data and plume measurements justify the selection of this working point and injection type. These data can be found at references [5, 6].

The transport variables at steady state output of HYPHEN (PIC-fluid modules) are first introduced in

Copyright 2024 by the Electric Rocket Propulsion Society. All rights reserved.

section 1. Subsequently, section 2 presents the analysis of the output of the wave module in terms of wave electric field components and power deposition maps for the two azimuthal modes $m = \pm 1$.

1. *Plasma transport*

Figure 4 shows the power deposition profile output of the W-module as seen by the electron fluid module. As will be discussed in detail in section 2, the majority of the power is coupled to the plasma within the discharge chamber, and only a residual fraction is absorbed in the plume. Within the PC itself, the regions of highest power absorption are near the resonance surface and close to the injector at the backplate. Figures 5a-5e illustrate that most of the ion production happens at the injection point due to both the high neutral density and sufficiently large electron temperature, resulting in the ion production region shown in figure 5b. Consequently, the plasma density, n, peaks close to the injector and decreases towards the axis and downstream. The density does not increase close to the resonance surface, despite more power being coupled there.

Due to the distributions of Q_a and n, the electron temperature peaks on the thruster axis, reaching up to 45 eV (refer to figure 5e). Conversely, a lower temperature is observed near the injection site, along the magnetic field lines connecting the backplate to the thruster's lateral walls. Despite some power deposition occurring also in this region, collisions and wall losses reduce the thermal energy available to the electrons. Overall, the high electron temperature obtained in this simulation significantly differs from the one measured in the experiments farther downstream in the plume [5, 6], which is $T_e = 4 - 6$ eV at $z = 130$ mm. This discrepancy could indicate cooling has taken place from the source to the measurement region, but could also indicate an overoptimistic simulation result.

As a result of the high electron temperature, the plasma potential (figure 5f) reaches a maximum of $\Phi \approx 240$ eV on the axis. The plasma potential also increases at large radii, outside of the PC. This phenomenon is due to the shape of the magnetic field and the significantly reduced mobility of electrons in the cross-field direction. However, not all ions will be accelerated through the maximum potential drop, as most are produced in regions with lower potential, which is clearly shown in Figure 6. The maximum ion energy reached in the domain is $E_i \approx 90$ eV, but they are expected to accelerate further as the plasma potential goes to zero at infinity. As a comparison for the same working point, measurements have shown total energies only up to $E_i = 65$ eV, a difference most probably driven by the higher electron temperature found for these simulations.

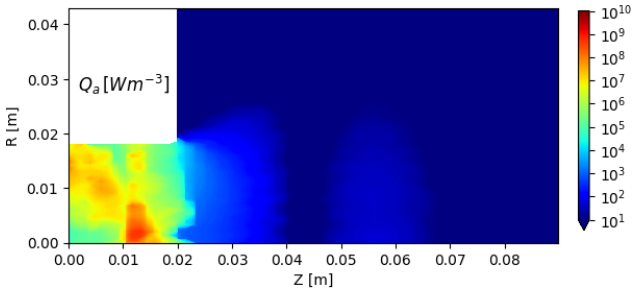

Figure 4: Power deposition map Q_a for the reference case as seen by the electron fluid module.

Copyright 2024 by the Electric Rocket Propulsion Society. All rights reserved.

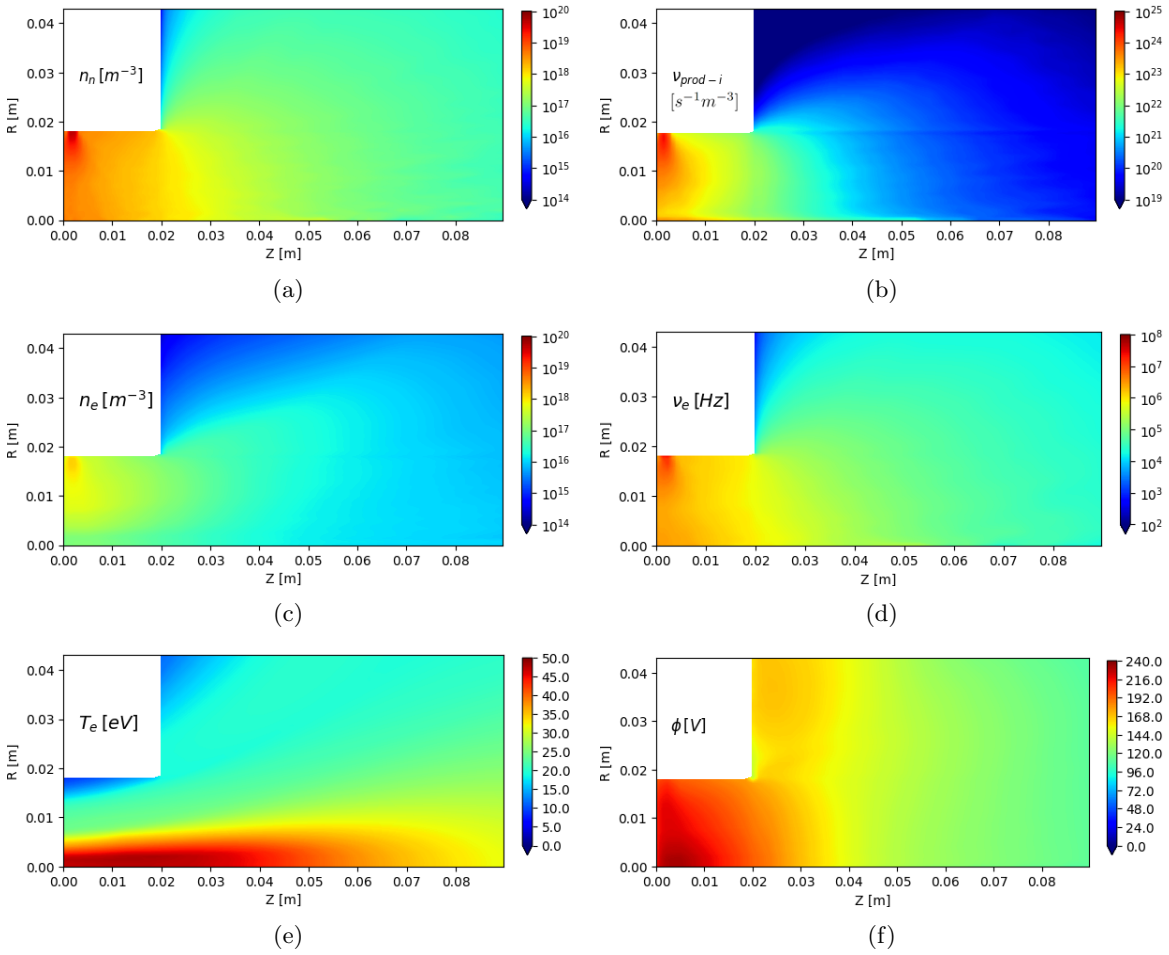

Figure 5: 2D maps of the main transport parameters for the reference case.

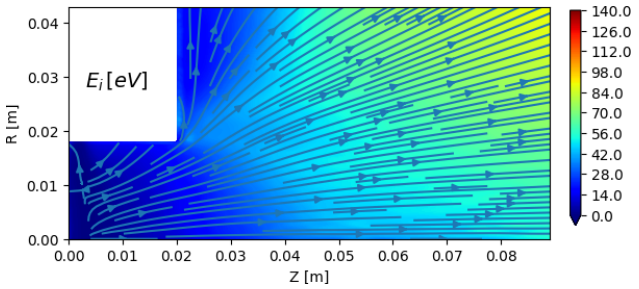

Figure 6: Ion energy map for the reference case, the streamlines represent the ion fluid velocity.

Prop. inj.	η_F [%]	η_{ene} [%]	η_{div} [%]	η_{disp} [%]	η_u [%]	η_{prod} [%]	P_{wall}/P_a [%]	P_{inel}/P_a [%]
Radial	4.5	20.3	58.4	38.4	35.3	17.5	71.1	8
Axial	15.3	48.2	51.7	61.4	80.9	57	47.3	2.4

Table 2: Table summarizing the global thruster performance for the two injection methods.

Table 2 shows the thruster performances. These indicators are defined based on the ion mass flow and

Copyright 2024 by the Electric Rocket Propulsion Society. All rights reserved.

Prop. inj.	P_{a+1}/P_a [%]	P_{a-1}/P_a [%]	Γ^2_{+1} [%]	Γ^2_{-1} [%]
Radial	55.7	44.3	32	46
Axial	86.6	13.4	41	90

Table 3: The power absorbed, and the power reflected fractions per microwave waveguide azimuthal mode (mode $m = \pm 1$) for the two injection methods.

power balances [14], which in the steady state are

$$\dot{m}_i = \dot{m}_{i,wall} + \dot{m}_{i,beam}, \tag{7}$$

and

$$P_a = P_{inel} + P_{wall} + P_{beam}. \tag{8}$$

In these expressions, $\dot{m}_{i,wall}$ and P_{wall} are the ion mass flow and plasma energy flow to the thruster walls (B3+B4), respectively; $\dot{m}_{i,beam}$ and P_{beam} are those to the free loss surface (B2); and P_{inel} is the power sink due to inelastic collisions. The propellant mass utilization and the ion production efficiency are defined, respectively, as

$$\eta_u = \dot{m}_{i,beam}/\dot{m}_p, \qquad \eta_{prod} = \dot{m}_{i,beam}/\dot{m}_i. \tag{9}$$

The thrust efficiency is defined as

$$\eta_F = \frac{F^2}{2\dot{m}_p P_a} \equiv \eta_{ene}\eta_{div}\eta_{disp}. \tag{10}$$

The energy, plume-dispersion, and plume-divergence efficiencies are, respectively,

$$\eta_{ene} = \frac{P_{beam}}{P_a}, \qquad \eta_{disp} = \frac{F^2}{2\dot{m}_p P^{(z)}_{beam}}, \qquad \eta_{div} = \frac{P^{(z)}_{beam}}{P_{beam}}, \tag{11}$$

Here F and $P^{(z)}_{beam}$ are the thrust and the plasma axial energy flow downstream.

The obtained thrust efficiency is only 4.5%, a value close to those found experimentally [5, 6]. As was seen in those previous works, also for these simulations the main factor limiting the thruster's performance is the energy efficiency reaching $\eta_e = 20\%$: up to 71% of power is deposited directly onto the thruster walls, and the remaining part is lost in inelastic collisions (e.g. ionization and excitation).

The dispersion efficiency is indicative of the dispersion of the velocities of all the species in the plasma beam. η_u/η_{prod} gives the total amount of ions produced per injected neutrals. For this simulation, this ratio is about 2. This result is indicative that every injected neutral is ionized once, it recombines at the walls after impact, and gets ionized once again. Therefore we should expect a large utilization efficiency [12, 14, 11]. However, it also means that on average, any subsequent recombination does not result in a re-ionization. It has been found that the accommodation factor for the recombined neutrals, plays a major role in the utilization efficiency. Hot/fast neutrals, having a longer mean free path, can more easily escape the domain without undergoing ionization, especially if they are produced from recombinations in proximity to the exit plane. With $\alpha_w = 0.8$, as in this work, a neutral temperature of up to $T_n = 3$ eV can be found in the PC. For comparison, $\alpha_w = 1$ (neutrals-wall thermalization) would lead to a maximum of $T_n = 0.1$ eV.

2. *Electromagnetic fields*

Figure 7 shows the electromagnetic wave propagating within the waveguide (in vacuum) positioned upstream of the discharge chamber. The electric field in the θ direction for mode $m = +1$ is evaluated at the axis and shown as a reference. A z-constant field magnitude would indicate a wave propagating purely in the forward direction (towards the right in this case). Instead, the field magnitude varies in this region and presents a minimum in the middle of the waveguide (refer to figure 7), indicating that some power is reflected towards the wave-port creating a standing wave. When a standing wave forms, the distance between the two nodes is half of the characteristic wavelength. In this case, $\lambda_{WG} = 0.095$ mm is measured, in agreement with half the wavelength of a wave with frequency $\omega = 5.8$ GHz, propagating in a vacuum within a waveguide of $D_T = 36$ mm.

Copyright 2024 by the Electric Rocket Propulsion Society. All rights reserved.

We measure that 32% and 46% of the forward power is reflected for mode $m = +1$ and mode $m = -1$, respectively, these values are shown in table 3. The amount of reflected power depends partially on the impedance mismatch caused by the plasma in the PC and plume indicating that not all the input (forward) power is absorbed. However note that as mentioned in section IIA, in this work the total absorbed power (sum of mode $m = \pm 1$) is prescribed to be $P_a = 175$ W, therefore the forward power needs to be re-scaled accordingly to meet this objective.

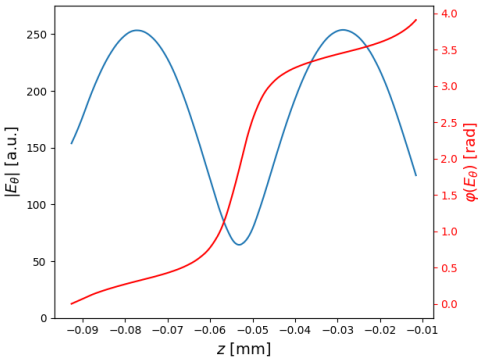

Figure 7: Magnitude and phase of the E_θ electric field component at $r = 0$ for mode $m = +1$.

As explained, having fixed the excitation frequency ω the solution for the propagation of EM waves in the plasma depends on the density n, collisionality ν, and magnetic field map B (refer respectively to figures 5c, 5d and 2). These quantities define regions in the plasma domain within which the EM wave can propagate, resonate, or show cut-offs. In this work we refer to these regions with the common nomenclature (from region I to VIII) adopted by [22] and [23].

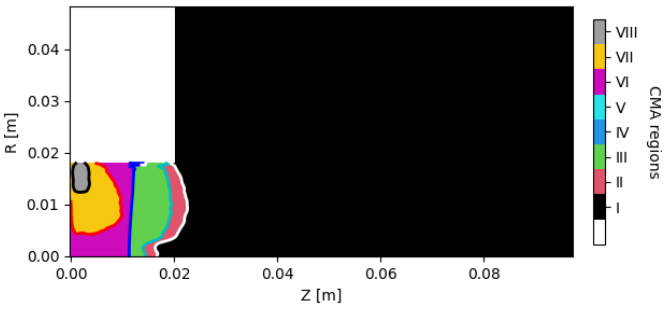

Figure 8: Regions of the CMA diagram obtained for the reference case.

Referring to figure 8, as the wave propagates from the left (waveguide) to the right (plume), it encounters decreasing density and magnetic field profiles. The resonance (blue solid line) separates regions VI–VIII (upstream) from regions I–V (downstream). The plasma is over-dense only in the region in proximity to the injection. As a result, the resonance is crossed with an under-dense plasma. These regions determine the patterns that can be found in the wave electric field solution. The latter are here presented for the two modes $m = \pm 1$ in figures 9 and 10. Figures 9-(a,c) and 10-(a,c) show the magnitude of the electric field components in the r, θ, and z directions, while figures 9-(d,f) and 10-(d,f) show their phase information.

In a circular waveguide of this size ($D_T = 36$ mm), and for the frequency 5.8 GHz, only the TE_{11} mode can propagate. Therefore, on the vacuum side, the electric field does not have any component in the z direction. On the other hand, this field component becomes, in general, nonzero in the presence of plasma, as shown in figure 9. The magnitude of the electric field components are larger in the PC if compared with the one in the waveguide or plume. Here the wave undergoes transitions between different regions and a variety of modes may be excited. With the help of figure 8, it can be observed that the largest electric field magnitudes appear in regions VIII, VII, and III, within which standing waves are found. Note that it is difficult if not impossible to discern each of these modes being the provided solution a superposition of all of them, possibly

Copyright 2024 by the Electric Rocket Propulsion Society. All rights reserved.

including multiple reflections at transitions lines and the metallic walls at the boundaries. As a consequence, we see an intricate pattern of interfering short-wavelengths ($\lambda \approx 10 - 20\mu$m) waves propagating in different directions as can be observed in figure 9-(d-f) and 10-(d-f).

Concerning the electric field magnitudes, another aspect of interest is the wave solution in the near plume region. For the injected mode $m = +1$ the electric field appears to be strongly damped outside of the discharge chamber, on the other hand, this effect is less important for the $m = -1$ mode, therefore electromagnetic power can still propagate in the plume (region I) and reach the boundaries of the domain. Here the power is reflected back by the metallic boundary condition downstream leading to a standing wave in the plume (not shown). Microwave radiation in the vacuum chamber has been observed for waveguide ECR thruster experiments [1, 5], but it is not typical of coaxial ECRTs. The fact that mode $m = -1$ can partially radiate, provides a possible explanation for this phenomenon. In the presence of a denser plasma (or at lower wave frequencies), the ECR would act as a very effective power confinement surface, preventing free space losses [12]. On the contrary, standing waves indicate that power is also propagating upstream, from the plume towards the PC, and due to the metallic BCs, artificially enhancing power absorption for mode $m = -1$. This highlights the current limit of the performed simulations, where a radiation boundary condition or a perfectly matched layer (PML) should be used instead of a metallic one.

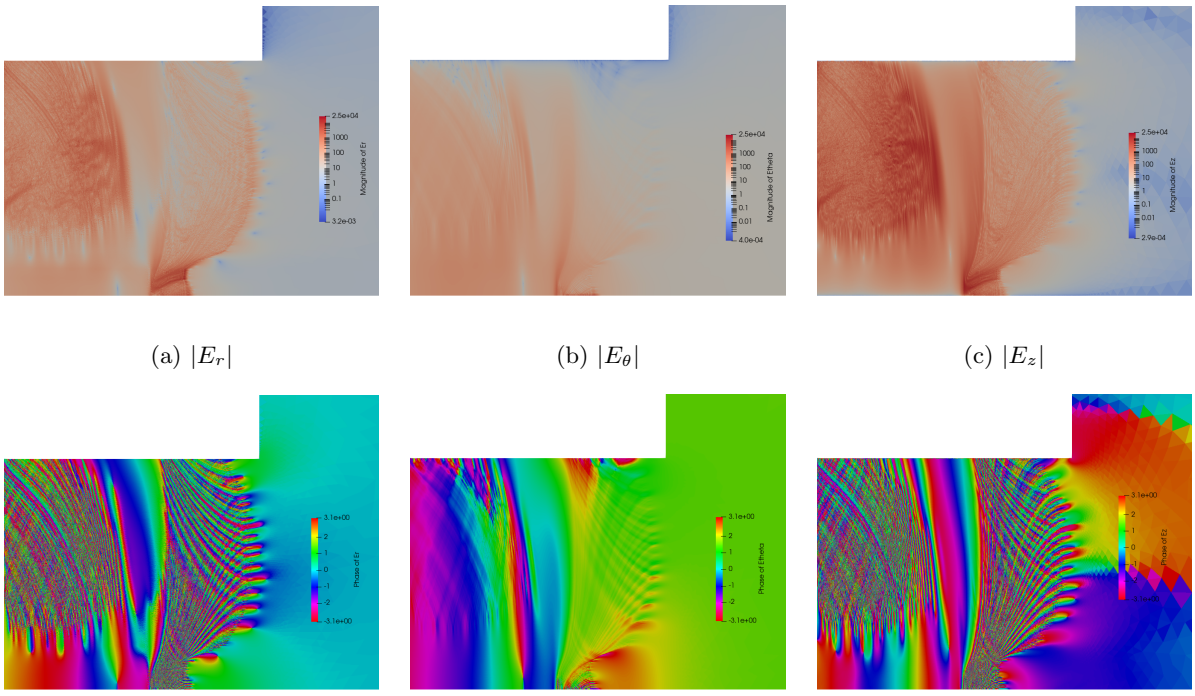

(a) $|E_r|$ (b) $|E_\theta|$ (c) $|E_z|$

(d) $\varphi(E_r)$ (e) $\varphi(E_\theta)$ (f) $\varphi(E_z)$

Figure 9: Electric field magnitudes and phases for $m = +1$.

Copyright 2024 by the Electric Rocket Propulsion Society. All rights reserved.

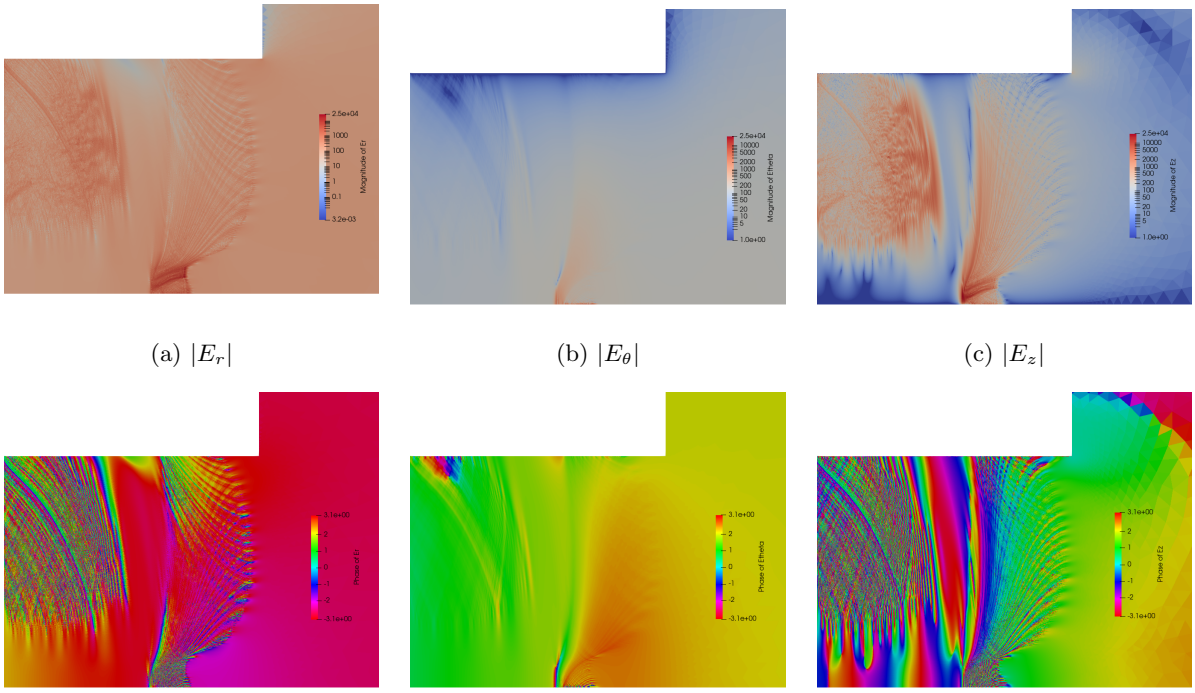

(a) $|E_r|$ (b) $|E_\theta|$ (c) $|E_z|$

(d) $\varphi(E_r)$ (e) $\varphi(E_\theta)$ (f) $\varphi(E_z)$

Figure 10: Electric field magnitudes and phases for $m = -1$.

Figure 11 represents the power absorption maps in the discharge chamber for modes $m = \pm 1$. As previously discussed, the effects produced by the resonant waves in regions III, VII, and VIII lead to significant power absorption in those areas. Absorption is also more pronounced near resonances, particularly at the thruster axis where the Upper Hybrid Resonance (UHR) and the Electron Cyclotron Resonance (ECR) converge.

Mode $m = +1$ and $m = -1$ are respectively of type Right Hand Polarized (RHP) and Left Hand Polarized (LHP) waves when injected in the waveguide at the wave-port. Therefore, and despite the fact that polarity changes may occur inside the plasma, $m = +1$ is expected to be predominantly linked to R waves within the PC and plume, which would then be absorbed in the resonance. Conversely, $m = -1$ would lead to L waves, which do not present any resonance, meaning power absorption should be limited for this mode.

However, the fraction of power absorbed is 55.7% and 44.3 % for mode $m = +1$ and $m = -1$ respectively (refer to table 3). The non-negligible amount of power absorbed shown for mode $m = -1$ may be explained by conversion between R and L waves, and vice versa. An additional contribution may come from the discussed larger amount of power radiated for mode $m = -1$. This power, normally radiated into free space, is reflected to the plasma source by the metallic boundary conditions positioned downstream, enhancing power absorption for this mode.

Copyright 2024 by the Electric Rocket Propulsion Society. All rights reserved.

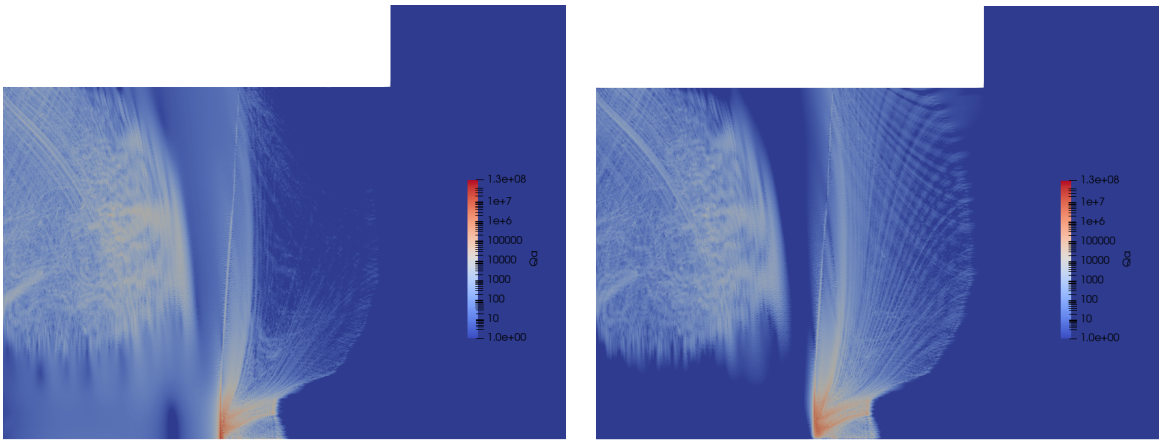

Figure 11: Power absorption profile Q_a for mode $m = +1$ (a) and mode $m = -1$ (b).

The short-wavelength patterns found in regions III, VII, and VIII, can be observed as well in figure 11. Two dominant directions of propagation are present, as shown by the iso-phase surfaces in figures 9-(d-f) and 10-(d-f). Regions III, VII, and VIII are all characterized by wave-normal surfaces presenting resonant cones at well-defined directions of propagation. It is found that these directions closely correspond to those identifiable in the phase plot. In the cold plasma model, the resonance cone angle can be obtained from the dispersion relation in the form of equation 12 [22], and taking a limit for $n \to \infty$ as in equation 13

$$\tan^2\theta = \frac{-P^2(n^2-R)(n^2-L)}{[(R+L)n^2-RL](n^2-P)} \tag{12}$$

$$\tan^2\theta_{res} = \lim_{n\to\infty} \tan^2\theta = \frac{-P}{R+L} \tag{13}$$

where θ_{res} is the resonance cone angle with respect to the magnetic field direction. This angle identifies the direction of propagation a wave should have to resonate. This direction is shown in figure 12 as red and blue vectors. The red and blue solid lines are perpendicular to these vectors and identify iso-phase surfaces. As it might be observed by comparing 12 and 9-(d-f) and 10-(d-f), there is a strong agreement between the iso-phase surfaces of a wave propagating in the direction of the resonance cone and those found in the solution of the electric field.

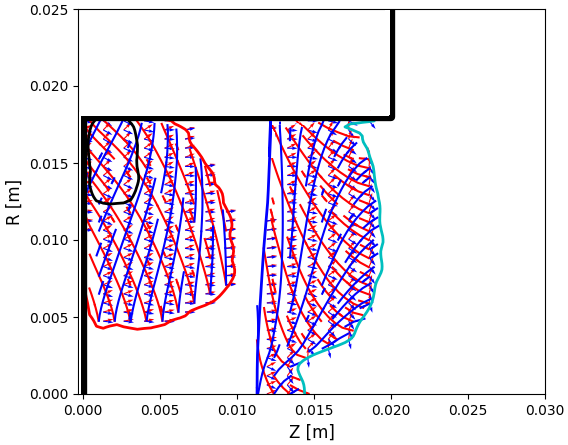

Figure 12: Quiver plot of the local resonance cone direction for the two θ_{res} solutions (red and blue vectors). The red and blue streamlines indicate the iso-phase surfaces of waves propagating in those directions.

Copyright 2024 by the Electric Rocket Propulsion Society. All rights reserved.

IIIB. Effect of axial injection

In the previous section, it has been shown that the high-density plasma region, regions VIII and VII, are characterized by large absorption of power. However, for the previous case, the latter are positioned at large radii, in proximity to the lateral walls and backplate, leading to substantial wall losses. In this section, the axial injection case is analyzed expected to partially limit these negative effects.

Referring to figure 13a, the neutral density is uniform in the discharge chamber , and is globally lower with respect to the radial scenario. Ionization happens mainly in proximity to the injection point as shown in figure 13b extending axially shortly outside of the discharge chamber. Consequently the density (figure 13c) shows a similar profile, a peak is present on the axis reaching values as high as $n_e = 10^{19}$ m^{-3} close to the injection point larger than the radial case, a sign that the recombination at the walls is reduced.

This density distribution in the PC results in the CMA regions shown in figure 13g and in the power absorption map in figure 13h. All regions are present in the domain, including regions IV and V which were previously absent. Region VIII is larger and positioned on the axis extending from the backplate up to the ECR. Consequently, region V can be found downstream of the ECR, in which no plasma wave can propagate, and therefore power absorption in this region is minimal. The over-dense plasma region is confined on the axis and extends up to $z = 40$ mm within the plume. The majority of power is absorbed in region VIII and at the ECR, but also for this case region III and the Upper Hybrid Resonance, which extends in the plume and up to the lateral walls, show a non-negligible absorbed power density.

The plasma density n decreases as we move towards higher radii in the PC, due to the non-negligible power absorption here, the power deposited per electron increases, increasing T_e up to about 40 eV leading to an off-axis peak (figure 13d). The plasma potential is shown in figure 13e, the potential peak is at $\Phi \approx 230$ V and is confined in a small volume at the injection in proximity to the backplate, however since most of the ions are also produced in this region (figure 13b), a large fraction of them have a larger potential drop available if compared to the radial injection (figure 14). An additional secondary peak can be found in the PC on the magnetic field lines corresponding to the peak of T_e.

Copyright 2024 by the Electric Rocket Propulsion Society. All rights reserved.

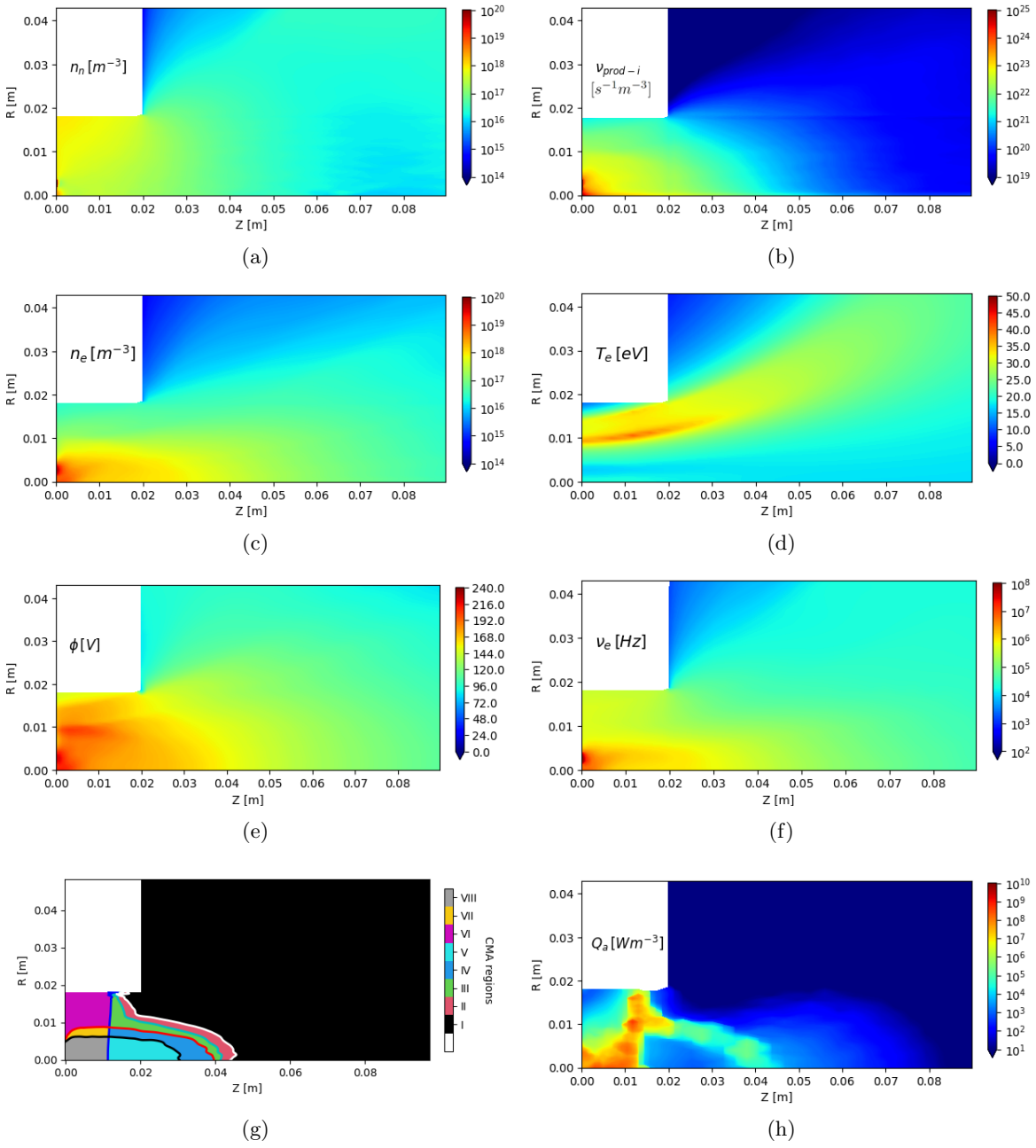

Figure 13: 2D maps of the main transport parameters for the axial propellant injection case.

Copyright 2024 by the Electric Rocket Propulsion Society. All rights reserved.

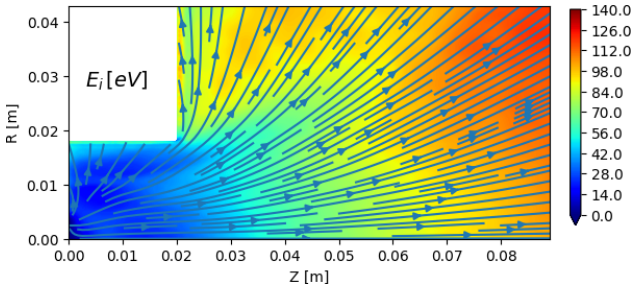

Figure 14: Ion energy map for the axial injection scenario, the streamlines represent the ion fluid velocity.

Referring to table 2, this propellant injection strategy brings substantial improvements in energy efficiency and dispersion efficiency, reaching respectively $\eta_{ene} = 48.2\%$ and $\eta_{disp} = 61.4\%$. η_{div}, on the other hand, is slightly negatively affected. Globally these improvements lead to a thrust efficiency, $\eta_T = 15.3\%$, which is more than three times larger than the one obtained for the reference case. The largest contribution to the performance improvement is brought by the reduced ion flux to the walls, this leads to: (i) a larger production efficiency, on average ions are now recombined less than one time; (ii) since the majority of lost neutrals come from recombination, the utilization efficiency is more than doubled; (iii) less recombination leads to less energy lost in re-ionizing neutrals, an energy that becomes available for ion acceleration.

Differences with respect to the reference case can also be observed concerning the absorption and reflection of the two modes $m = \pm 1$. Referring to table 3, for both modes the power reflection level is increased, with $\Gamma^2_{+1} = 41\%$ and $\Gamma^2_{-1} = 90\%$ respectively. Nearly all of the power for mode $m = -1$ is reflected. As previously discussed, mode $m = -1$ is expected to be mainly associated with an L wave, the latter cannot propagate in region VIII which is positioned just downstream of the backplate, therefore this power is reflected back to the waveguide. This results in the $m = -1$ mode contributing only to 13.4% of the total absorbed power.

IV. Conclusions

With the objective of simulating the plasma discharge of a waveguide ECR thruster, a hybrid PIC-fluid model coupled with a frequency domain, cold-plasma wave code has been used to compute, the wave-propagation and electromagnetic power absorption by the plasma. The analysis yields the plasma properties and wave propagation and absorption maps for two scenarios: when the propellant injection is radial, and when it is axial. For both cases, the $m = \pm 1$ modes were injected at the wave-port.

Injecting the propellant radially is seen to lead to substantial losses to the thruster walls, where up to 70% of power is lost, largely decreasing the energy available for ion acceleration. The ions recombining at the walls have a longer mean free path than the injected neutrals, and manage to escape the source. This leads to a rather low utilization efficiency. The output from the wave module showed that CMA regions III, VII, and VIII are associated with the largest volumetric power absorption, linked to the presence of shorter wavelengths there. Most of the power is deposited in proximity to the axis but also close to the injection (region VIII). Mode $m = +1$ deposits more power into the plasma, presenting a lower power reflection level with respect to mode $m = -1$.

The axial injection in proximity to the axis partially solves these problems. The power fluxes to the walls are reduced by 20% and a lower amount of ions are recombined, increasing the utilization efficiency up to 80%. The different plasma density profile obtained leads to different patterns of power absorption and response for the two injected modes. Mode $m = -1$ couples less power since the majority is reflected. This has been attributed to the presence of a large region VIII on the thruster axis, hinting that impedance matching can be necessary when this propellant injection strategy is followed.

The work conducted serves as a foundational step in understanding wave propagation and power absorption in waveguide ECR thrusters, pointing out several aspects that warrant further research. Numerical investigations and a convergence analysis are needed to rule out possible issues and the presence of spurious solutions in the wave solution, particularly, in the presence of resonance cones as is the case. Understanding better the wave behavior near critical transitions, including power absorption, reflections, and polarity changes is also the object of ongoing research. Additionally, it was observed that power can radiate out of the discharge chamber and be reflected back by the metallic boundary conditions downstream, particularly for

Copyright 2024 by the Electric Rocket Propulsion Society. All rights reserved.

mode $m = -1$. This highlights the necessity for improved boundary conditions at the downstream surfaces, such as a radiation boundary or a perfectly matched layer. Furthermore, intending to obtain a clear picture of the discharge chamber physics, it is of interest to fine-tune the transport model free parameters with the available experimental data, this is particularly true for the electron temperature found, for which it was shown that the discrepancy with experiments is significant.

Finally, the analysis revealed that axial injection could potentially enhance the performance of a waveguide ECR thruster. Consequently experimentally testing this possibility will be the subject of future works.

Acknowledgments

The contribution of the authors M. R. Inchingolo and J. Navarro-Cavallé has been supported by the R&D project TED2021-132484B-I00 (SUPERLEO) funded by MCIN/AEI/10.13039/501100011033 and by "European Union NextGenerationEU/PRTR". The contribution of P. Jimenez and M. Merino has been supported by the European Research Council (ERC) under the European Union's Horizon 2020 research and innovation program, project ZARATHUSTRA, (grant agreement No 950466). J. Zhou has been supported by the program *Recualificación del Sistema Universitario Español, Margarita Salas*, of the Ministerio de Universidades (Spanish Government)

References

[1] G.F. Crimi, A.C. Eckert, and DB Miller. *Microwave Driven Magnetic Plasma Accelerator Studies (Cyclops)*. Tech. rep. General Electric Company, Space Sciences Laboratory, Missile and Space Division, 1967.

[2] J.C. Sercel. "An experimental and theoretical study of the ECR plasma engine". PhD thesis. California Institute of Technology, 1993.

[3] F. Cannat, T. Lafleur, J. Jarrige, P. Chabert, P.Q. Elias, and D. Packan. "Optimization of a coaxial electron cyclotron resonance plasma thruster with an analytical model". In: *Physics of Plasmas* 22.5 (2015), p. 053503.

[4] Victor Désangles et al. "ECRA Thruster Advances: 30W and 200W Prototypes Latest Performances". In: *Journal of Electric Propulsion* 2.1 (2023), p. 10. DOI: 10.1007/s44205-023-00046-x.

[5] M. R. Inchingolo, M. Merino, and J. Navarro-Cavallé. "Plume Characterization of a Waveguide ECR Thruster". In: *Journal of Applied Physics* 133.11 (2023), p. 113304. DOI: 10.1063/5.0138780.

[6] M. R. Inchingolo, M. Merino, M. Wijnen, and J. Navarro-Cavallé. "Thrust Measurements of a waveguide Electron Cyclotron Resonance Thruster". In: *Journal of Applied Physics* 135.9 (Mar. 2024). DOI: 10.1063/5.0186778. URL: https://doi.org/10.1063/5.0186778.

[7] T. Lafleur. "Helicon plasma thruster discharge model". In: *Physics of Plasmas* 21.4 (2014), p. 043507.

[8] A. Domínguez-Vázquez. "Axisymmetric simulation codes for Hall effect thrusters and plasma plumes". PhD thesis. Universidad Carlos III de Madrid, Leganés, Spain, 2019.

[9] Jiewei Zhou. "Modeling and simulation of the plasma discharge in a radiofrequency thruster". PhD thesis. Universidad Carlos III de Madrid, Leganés, Spain, 2021.

[10] A. Sánchez-Villar, J. Zhou, M. Merino, and E. Ahedo. "Coupled plasma transport and electromagnetic wave simulation of an ECR thruster". In: *Plasma Sources Science and Technology* 30.4 (2021), p. 045005. DOI: 10.1088/1361-6595/abde20.

[11] Marco Riccardo Inchingolo, Mario Merino, and Jaume Navarro-Cavallé. "Hybrid PIC-Fluid Simulation of a Waveguide ECR Magnetic Nozzle Plasma Thruster". In: *Space Propulsion Conference 2021*. 00192. March 17-19: Association Aéronautique et Astronautique de France, 2021.

[12] Pedro Jiménez, Jiewei Zhou, Jaume Navarro-Cavallé, Pablo Fajardo, Mario Merino, and Eduardo Ahedo. "Analysis of a cusped helicon plasma thruster discharge". In: *Plasma Sources Science and Technology* 32.10 (2023), p. 105013. DOI: 10.1088/1361-6595/ad01da.

[13] A. Domínguez-Vázquez, F. Cichocki, M. Merino, P. Fajardo, and E. Ahedo. "Axisymmetric plasma plume characterization with 2D and 3D particle codes". In: *Plasma Sources Science and Technology* 27.10 (2018), p. 104009. DOI: 10.1088/1361-6595/aae702.

Copyright 2024 by the Electric Rocket Propulsion Society. All rights reserved.

[14] J. Zhou, A. Domínguez-Vázquez, P. Fajardo, and E. Ahedo. "Magnetized fluid electron model within a two-dimensional hybrid simulation code for electrodeless plasma thrusters". In: *Plasma Sources Science and Technology* 31.4 (2022), p. 045021.

[15] Jiewei Zhou, Daniel Pérez-Grande, Pablo Fajardo, and Eduardo Ahedo. "Numerical treatment of a magnetized electron fluid within an electromagnetic plasma thruster code". In: *Plasma Sources Science and Technology* 28.11 (2019), p. 115004.

[16] Jesús Perales-Díaz et al. "Hybrid plasma simulations of a magnetically shielded Hall thruster". In: *Journal of Applied Physics* 131.10 (2022), p. 103302. DOI: 10.1063/5.0065220.

[17] Jian-Ming Jin and Douglas J Riley. *Finite element analysis of antennas and arrays*. John Wiley & Sons, 2009.

[18] Jean-Claude Nédélec. "Mixed finite elements in R^3". In: *Numerische Mathematik* 35.3 (1980), pp. 315–341.

[19] Peter Monk. *Finite element methods for Maxwell's equations*. Oxford University Press, 2003.

[20] Adrián Domínguez-Vázquez, Jiewei Zhou, Alejandro Sevillano-González, Pablo Fajardo, and Eduardo Ahedo. "Analysis of the electron downstream boundary conditions in a 2D hybrid code for Hall thrusters". In: 37^{th} *International Electric Propulsion Conference*. IEPC-2022-338. Boston, MA, June 19-23: Electric Rocket Propulsion Society, 2022.

[21] A. Domínguez-Vázquez, F. Cichocki, M. Merino, P. Fajardo, and E. Ahedo. "On heavy particle-wall interaction in axisymmetric plasma discharges". In: *Plasma Sources Science and Technology* 30.8 (Aug. 2021), p. 085004. DOI: 10.1088/1361-6595/ac1715.

[22] Thomas H Stix. *Waves in plasmas*. Springer Science & Business Media, 1992.

[23] J.A. Bittencourt. *Fundamentals of plasma physics*. Springer, Berlin, Germany, 2004.

Copyright 2024 by the Electric Rocket Propulsion Society. All rights reserved.